

Predicting crystals of Janus colloids

Teun Vissers,^{1,2,a)} Zdeněk Preisler,^{1,a)} Frank Smallenburg,¹ Marjolein Dijkstra,² and Francesco Sciortino¹

¹Dipartimento di Fisica, Sapienza Università di Roma, Piazzale Aldo Moro 5, 00185 Roma, Italy

²Soft Condensed Matter, Debye Institute for Nanomaterials Science, Utrecht University, Princetonplein 5, 3584 CC Utrecht, The Netherlands

(Received 7 February 2013; accepted 12 March 2013; published online 26 April 2013)

We present a numerical study on the phase diagram for a simple model of Janus colloids, including ordered and disordered structures. Using a range of techniques, we generate a set of crystal structures and investigate their relative stability field in the pressure-temperature and temperature-density planes by means of free-energy calculations and thermodynamic integration schemes. We find that despite the Janus colloids' simple architecture, they form stable crystal structures with complicated bond-topologies on an underlying face-centered-cubic or hexagonal-close-packed lattice. In addition, we find a phase consisting of wrinkled bilayer sheets, competing with both the fluid and the crystal phases. We detect a metastable gas-liquid coexistence which displays a micellization-driven re-entrant behavior. © 2013 AIP Publishing LLC. [<http://dx.doi.org/10.1063/1.4801438>]

INTRODUCTION

The need for new functional materials spurred scientific progress in the design and synthesis of colloidal particles with well-defined shapes and interactions.^{1,2} The particle surface can be chemically modified to create attractive patches, resulting in directional interactions.^{3–5} These so-called “patchy particles,” which can be investigated in computer simulations with surprisingly simple models,^{6–8} have been shown to form several interesting structures such as micelles, vesicles, tubes, and sheets.^{9–12}

Recent work has shown that such models are extremely powerful, and even applicable to more complex experimental systems such as gels of clay-platelets,^{13,14} and to particles with more than one type of patch on their surface.^{15–17} In particular, there has been interest in the design and stability of patchy colloidal crystals since these show a high potential for future photonic applications.¹⁸ Moreover, colloids are excellent experimental model systems, since they can be easily studied with confocal microscopy.¹⁹

To numerically determine the complete phase diagram of a model, including both ordered and disordered phases, two main steps are necessary: (i) create a list of all possible (crystal) structures and (ii) evaluate their chemical potential as a function of temperature T , and pressure P . While methodologies for evaluating crystal free energies are nowadays well-developed,²⁰ finding the candidate lattices is still the subject of ongoing research. For hard particles, a novel “floppy box” Monte Carlo method was recently developed by Filion *et al.*²¹ where the simulation box can change both its shape as well as its volume during the simulation. By using a small number of particles (typically 1–12), unit-cell candidates can be generated at relatively low computational cost. The shape fluctuations allow to find crystal structures that do not fit in a cubic box. Recently, this method was extended to other, irregularly

shaped, hard particles.^{22–26} For completion, we note that one limitation of these methods is that quasi-crystals²⁷ cannot be directly identified in this way.

For patchy particles, most of the previous studies of crystal phases relied on an “educated guess” of crystal candidates.^{28–31} Only recently, genetic algorithms^{32,33} and floppy box methods³⁴ have been extended to patchy colloids in the attempt to generate a list of possible ground-state structures in a systematic way.

Here, we focus on Janus particles,^{35–44} i.e., colloidal spherical particles whose surface is divided evenly into two areas of different chemical composition, providing the most elementary and geometrically simple example of a surfactant particle,⁴⁵ in which solvophilic and solvophobic areas reside on different parts of the surface of the same particle. Some proteins, e.g., hydrophobin⁴⁶ and casein,⁴⁷ have large hydrophobic patches on their surface, similar to Janus colloids. The spontaneous organization of Janus colloids in finite size clusters has received considerable attention.^{48–52} It has been shown that these particles can form small-size aggregates, resembling micelles, and vesicles.

To our knowledge, no detailed studies have been dedicated to the complete phase diagram, including the crystal phases, of Janus particles neither experimentally nor numerically. Here, we do so, employing the well established one-patch Kern-Frenkel (KF) potential,⁵³ which models the repulsive hemisphere as a hard-core interaction and the attractive one via a square-well potential, with a range equal to 20% of the particle diameter. The two-patch analogue of this model has been validated against experiments and has shown to successfully describe the thermodynamics and self-assembly of triblock Janus particles in 2D,⁷ as well as the fluid state in 3D.⁵⁴ From the large number of candidate structures generated by the floppy box procedure, we select the few lattices which are stable in a selected region of the T - ρ plane and evaluate their coexistence lines, providing a complete picture of the model phase diagram. Here, we define the number

^{a)}T. Vissers and Z. Preisler contributed equally to this work.

density $\rho = N/V$, with N the number of particles, and V the volume of the system. The thermodynamically stable crystals we found are all formed by an underlying face-centered cubic (fcc) or hexagonal-close-packed (hcp) lattice, but with specific orientations of the particles. We found only one low-density periodic structure, in the form of a wrinkled bilayer, coexisting with a dilute, gaseous phase, and with orientationally ordered crystals.

We also calculated the stability field of the gas (colloid poor) and of the liquid (colloid rich) phases. A previous study of the same model, but for a relatively large attraction range (50% of the particle diameter), had revealed that a cluster phase of micelles forms at low temperature, which progressively gains stability with respect to the liquid phase.⁵⁵ Here, we show that the resulting re-entrant gas-liquid coexistence is also found in this model. However, the gas-liquid coexistence is found to be metastable with respect to a broad two-phase coexistence region of wrinkled bilayer-sheets and a fluid phase.

MODEL AND METHODS

The model

We select the Kern-Frenkel potential⁵³ (u^{KF}) as a simple model for non-overlapping, attractive Janus particles. u^{KF} is defined as

$$u^{\text{KF}}(\mathbf{r}_{ij}, \hat{\mathbf{n}}_i, \hat{\mathbf{n}}_j) = u^{\text{SW}}(r_{ij})\Omega(\mathbf{r}_{ij}, \hat{\mathbf{n}}_i, \hat{\mathbf{n}}_j), \quad (1)$$

where $u^{\text{SW}}(r_{ij})$ is a square-well interaction potential and $\Omega(\mathbf{r}_{ij}, \hat{\mathbf{n}}_i, \hat{\mathbf{n}}_j)$ is a function depending on orientations of two interacting particles:

$$u^{\text{SW}}(r_{ij}) = \begin{cases} \infty & \text{if } r_{ij} < \sigma \\ -\epsilon & \text{if } \sigma < r_{ij} < \sigma + \Delta \\ 0 & \text{if } r_{ij} > \sigma + \Delta, \end{cases} \quad (2)$$

where σ is the hard-sphere particle diameter and Δ is the interaction range of the square well attractions:

$$\Omega(\mathbf{r}_{ij}, \hat{\mathbf{n}}_i, \hat{\mathbf{n}}_j) = \begin{cases} 1 & \text{if } \begin{cases} \hat{\mathbf{r}}_{ij} \cdot \hat{\mathbf{n}}_i > \cos \theta \text{ and} \\ \hat{\mathbf{r}}_{ji} \cdot \hat{\mathbf{n}}_j > \cos \theta \end{cases} \\ 1 & \text{if } r_{ij} < \sigma \\ 0 & \text{otherwise,} \end{cases} \quad (3)$$

with $\hat{\mathbf{r}}_{ij}$ a unit vector pointing along the line joining the center of particles i and j , and $\hat{\mathbf{n}}_i$ and $\hat{\mathbf{n}}_j$ are the unit vectors indicating the orientations of particle i and j . The choice of $\cos(\theta) = 0$ corresponds to a coverage of 50%, i.e., to the Janus case. A schematic representation of two Janus particles interacting with this potential is given in Fig. 1. This model is able to reasonably reproduce the physical behavior of colloids with one hydrophobic and one hydrophilic hemisphere.⁴³ The well depth ϵ fixes the energy scale. The interaction range $\Delta = 0.2\sigma$ was chosen such that the coordination shell of the particles includes only nearest neighbors.

Finding crystals in a floppy box

To find crystal structure candidates, we used the variable box shape simulation strategy from Refs. 21 and 34. We per-

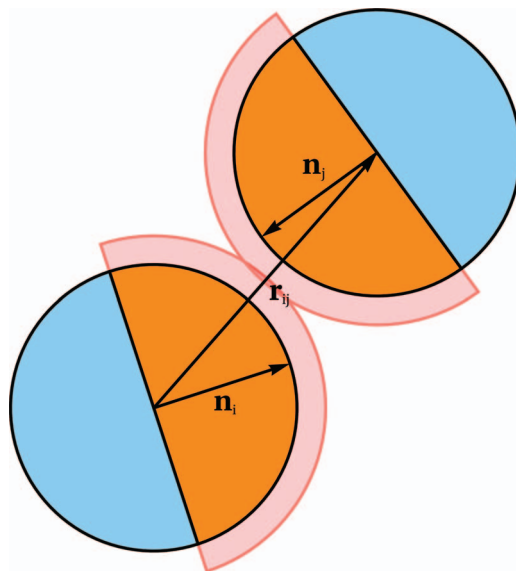


FIG. 1. Schematic 2D representation of two Janus spheres labeled i and j , interacting with a Kern-Frenkel potential as defined in Eq. (1). The attractive hemispheres are depicted in orange. The vector \mathbf{r}_{ij} points from particle i to particle j . The vectors $\hat{\mathbf{n}}_i$ and $\hat{\mathbf{n}}_j$ denote the orientations of particles i and j , respectively. The light red area indicates the range of the interaction, $\Delta = 0.2\sigma$ in this work. Note that this range corresponds to two times the width (in the radial direction) of the light red zone attached to a single particle.

formed simulations at constant pressure $P^* = P\sigma^3/k_B T$ and temperature $T^* = k_B T/\epsilon$ for different numbers of Janus particles $N = \{2, 3, \dots, 8\}$ in a small floppy simulation box. Here, k_B denotes the Boltzmann constant. The lengths of the vectors that span the box and the angles between them were allowed to fluctuate. For each value of N , we performed the simulation 20 times with a different random seed. Each simulation was started with a random configuration in the fluid state. Typically, we used $\mathcal{O}(10^7)$ rotation and translation moves per particle, and adjusted the shape and dimensions of the box every N MC moves. The step sizes were calibrated such that the acceptance probabilities were close to 50%. After the simulations were completed, we selected the configurations from the small floppy box with the highest number of bonds. These configurations, providing the unit cell, were multiplied a number of times in three directions to generate a larger crystal configuration. Subsequently, the resulting structure was equilibrated, always in a floppy box containing between 100 and 1000 Janus particles. Because some of these simulations yielded the same candidate (not necessarily in the same box-shape), we looked for a similarity in structure. To this end, we compared the average potential energy, average density, pair-correlation function, and orientation distribution function (Appendix A).

Crystal free energies

After identifying and classifying our structures, we performed free-energy calculations in order to predict their stability and draw the phase diagram. The phases under consideration are the fluid, sheets consisting of wrinkled bilayers, and several crystal structures (Fig. 2). To calculate the absolute free energy of the crystal phases we used the Frenkel-Ladd method.⁵⁶ Although there is plenty of literature on the

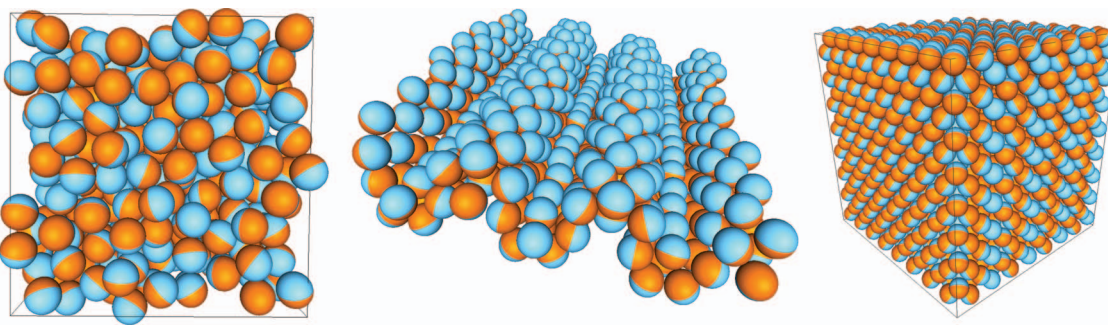


FIG. 2. Free-energy calculations were performed for Janus particles in a fluid (left), wrinkled bilayer sheets (middle), and crystals (right). The blue hemispheres have a hard-sphere character. The orange hemispheres are impenetrable as well, but in addition form attractive bonds, described by a square-well Kern-Frenkel attraction with range $\Delta = 0.2\sigma$.

subject,^{20,57} we will briefly discuss the procedures that we employed. Here, the reference system is an Einstein crystal with fixed center of mass. The particles inside the Einstein crystal are coupled to their lattice positions with a potential that depends on coupling parameter λ_{tr} . The particle orientations are coupled with a parameter λ_{or} . The total reference energy inside the Einstein crystal is the sum of the translational and the orientational reference Hamiltonians:

$$\mathcal{H}_{\text{ref}}(\lambda_{\text{tr}}, \lambda_{\text{or}}) = \mathcal{H}_{\text{ref}}^{\text{tr}}(\lambda_{\text{tr}}) + \mathcal{H}_{\text{ref}}^{\text{or}}(\lambda_{\text{or}}). \quad (4)$$

The translational reference Hamiltonian is

$$\mathcal{H}_{\text{ref}}^{\text{tr}}(\lambda_{\text{tr}}) = \lambda_{\text{tr}} \sum_{i=1}^N \frac{(|\mathbf{r}_i - \mathbf{r}_{i,0} - \mathbf{r}_{\text{cm}}|)^2}{\sigma^2}, \quad (5)$$

where \mathbf{r}_i is the position of a particle i , $\mathbf{r}_{i,0}$ the location of its spring-well, λ_{tr} is the translational coupling parameter, and \mathbf{r}_{cm} is the position of the center of mass of the whole system. The last term \mathbf{r}_{cm} is there to account for the collective drift of the whole crystal. The reference rotational Hamiltonian can be chosen arbitrarily but must have the same symmetry as the coupled system. To match the symmetry of the Janus particles, we employ an orientational ($C_{\infty v}$ -symmetric) Hamiltonian that reads

$$\mathcal{H}_{\text{ref}}^{\text{or}}(\lambda_{\text{or}}) = \lambda_{\text{or}} \sum_{i=1}^N (1 - \cos(\psi)), \quad (6)$$

where λ_{or} is the orientational coupling parameter, and ψ is the angle between the orientation of the particle and the orientation inside the Einstein crystal. During the simulations in the free-energy calculations, the particles feel a potential \mathcal{H}' that is the sum of the original Hamiltonian of the particles $\mathcal{H} = \sum_{i,j>i}^N u^{KF}(\mathbf{r}_{ij}, \hat{\mathbf{n}}_i, \hat{\mathbf{n}}_j)$, plus the reference Hamiltonian \mathcal{H}_{ref} :

$$\mathcal{H}' = \mathcal{H} + \mathcal{H}_{\text{ref}}(\lambda_{\text{tr}}, \lambda_{\text{or}}). \quad (7)$$

In this work, the positions and orientations are coupled with the same sample parameter, i.e., $\lambda = \lambda_{\text{or}} = \lambda_{\text{tr}}$. In the following we define for the potential energy U and the total free energy F :

$$f = \frac{F}{N}, \quad u = \frac{U}{N}, \quad (8)$$

where N is the number of particles, f is the free energy per particle, and u is the potential energy per particle. The free

energy can be evaluated by coupling the system of interest to a reference system with a known free energy. The difference between the investigated system and the reference system is then given by

$$\Delta f = f(0) - f(\lambda_{\text{max}}) = - \int_0^{\lambda_{\text{max}}} \left\langle \frac{d\mathcal{H}_{\text{ref}}(\lambda)}{d\lambda} \right\rangle_{N,V,T,\lambda} d\lambda, \quad (9)$$

where λ_{max} is a large value of the coupling parameter for which all the particles are fixed to their ideal positions and orientations in the Einstein crystal, such that the reference Hamiltonian is dominant and all the particles are coupled to the Einstein lattice. The absolute value for the free energy of the real system is the sum of the following contributions:

$$f = \Delta f + u_{\text{en}} + f_{\text{ref}}, \quad (10)$$

where Δf is given by Eq. (9), u_{en} is the Madelung-energy per particle in the perfect Einstein crystal, and f_{ref} is the free energy of the reference system, which consists of a translational and orientational part:

$$f_{\text{ref}}(\lambda_{\text{max}}) = f_{\text{ref}}^{\text{tr}}(\lambda_{\text{max}}) + f_{\text{ref}}^{\text{or}}(\lambda_{\text{max}}). \quad (11)$$

From Ref. 20, the translational free energy of an Einstein crystal with fixed center of mass is given by

$$\beta f_{\text{Ein}}^{\text{tr}}(\lambda_{\text{max}}) = -\frac{1}{N} \ln \left[\left(\frac{1}{\Lambda_t} \right)^{3N} \left(\frac{\pi \sigma^2}{\beta \lambda_{\text{max}}} \right)^{3(N-1)/2} N^{1/2} V \right], \quad (12)$$

where $\beta = 1/k_B T$, and $\Lambda_t = h / \sqrt{(2\pi m k_B T)}$, with h Planck's constant, and m the mass of a particle. For the orientational free energy of the reference system we use

$$\beta f_{\text{ref}}^{\text{or}}(\lambda_{\text{max}}) = -\ln \frac{1}{\Lambda_r} \frac{1 - e^{-2\beta\lambda_{\text{max}}}}{2\beta\lambda_{\text{max}}}. \quad (13)$$

where $\Lambda_r = h^2 / (8\pi^2 I k_B T)$ and I the moment of inertia of a Janus particle. A derivation is given in Appendix B. In the following we choose $\Lambda^3 = \Lambda_t^3 \Lambda_r = \sigma^3$ as the thermal volume. Please note that the coexistence lines are independent of the choice of Λ_t and Λ_r . The absolute free energy can now be calculated using Eq. (10). To evaluate Δf (Eq. (9)) we performed a series of NVT -simulations for different values of $\lambda = \lambda_{\text{or}} = \lambda_{\text{tr}}$, evaluating the average of $d\mathcal{H}_{\text{ref}}/d\lambda$. Subsequently, we

fitted a spline using Akima-interpolation⁵⁸ and integrated over this spline, rewriting the integral in Eq. (9) as

$$\Delta f = - \int_{\ln c}^{\ln \lambda_{\max} + c} \lambda \left(\frac{d\mathcal{H}_{\text{ref}}(\lambda + c)}{d\lambda} \right)_{N, V, T, \lambda_{\text{tr}}, \lambda_{\text{or}}} d(\ln \lambda + c), \quad (14)$$

where c is a small value up to where the integral of the reference Hamiltonian has a negligible contribution. Since a convenient choice for the Einstein crystal is important, we elaborate on this in Appendix C.

To evaluate the wrinkled bilayer reference free energy, we applied the Einstein crystal methodology to a rather dense configuration, such that the center of mass of the individual sheets does not diffuse.

Equations of state

The equations of state $P(\rho)$ of the different crystals were calculated via multiple series of *NPT*-simulations in a floppy box. For the fluid, a cubic box was used. In the case of the wrinkled bilayer sheets we had to take special care to avoid strong finite-size effects related to the translational entropy of the individual sheets. To this end, we implemented shifted boundary conditions to connect the individual bilayer sheets. To improve statistics, we employed a scheme using volume trial moves, similar to the pressure evaluation at constant volume described in Ref. 59. However, at very low pressures $P\sigma^3/k_B T \ll 0.01$ where particles in two adjacent sheets interact only sporadically, resolving the equation of state becomes computationally expensive and depends on different finite-size effects related to the curvature fluctuations of the sheets.

Determining the coexistence lines between different phases

From the free energy $F(\rho_1, T)$ evaluated via the Einstein crystal method, we calculated the free energy $F(\rho_2, T)$, at density ρ_2 via

$$\frac{F(\rho_2, T)}{Nk_B T} = \frac{F(\rho_1, T)}{Nk_B T} + \int_{\rho_1}^{\rho_2} \frac{P(\rho)}{k_B T \rho^2} d\rho. \quad (15)$$

The chemical potential $\mu(\rho_2, T)/Nk_B T$ can be determined by simply adding the term $P(\rho_2)/\rho_2 k_B T$. Alternatively, one can calculate along a constant pressure P path the Gibbs free energy $G(T, P) \equiv F + PV$. In this case, from the original state point $G(T_1, P)$, one obtains $G(T_2, P)$:

$$\frac{G(T_2, P)}{Nk_B T_2} = \frac{G(T_1, P)}{Nk_B T_1} + \int_{T_1}^{T_2} \frac{H(T)}{Nk_B T^2} dT, \quad (16)$$

where $H = U + PV$. In this case $\mu(T, P) = G(T, P)/N$.

Coexistence is defined by the intersection of the chemical potential of distinct phases along a constant T or a constant- P path. In this way, we establish the most stable crystal phases among all the candidate crystal structures, i.e., those with the lowest chemical potential for given $\{P, T\}$.

From the coexistence points, the coexistence lines can be obtained using the method of Kofke,⁶⁰ i.e., by integrating the

Clausius-Clapeyron equation:

$$\left(\frac{dP}{dT} \right)_{\text{coex}} = \frac{s_{\text{II}} - s_{\text{I}}}{v_{\text{II}} - v_{\text{I}}} = \frac{h_{\text{II}} - h_{\text{I}}}{T(v_{\text{II}} - v_{\text{I}})}, \quad (17)$$

where s_{I} and s_{II} denote the entropy per particle of two coexistence phases, labeled as I and II, v_{I} and v_{II} are the corresponding volumes per particle, and h_{I} and h_{II} are the enthalpy values per particle. We employed a fourth-order Runge-Kutta predictor-corrector scheme⁶¹ to perform the integration.

Thermodynamic integration at constant density

The free energy of the fluid can be calculated using thermodynamic integration over β at constant density and adding the hard-sphere contribution. We evaluate the hard-sphere contribution of the free energy using the Carnahan-Starling equation:⁶²

$$\beta f_{\text{HS}} = \ln(\rho \Lambda^3) - 1 + \frac{4\eta - 3\eta^2}{(1 - \eta)^2}, \quad (18)$$

where Λ^3 is the thermal volume of a single particle, and η is the packing fraction and $\rho = N/V$ the density. The free energy becomes

$$\beta f_{\text{int}} = \beta f_{\text{HS}} + \int_0^\beta \langle u_{\text{int}}(\beta') \rangle_{\beta'} d\beta', \quad (19)$$

where the integrand is evaluated using constant *NVT*-simulations starting at high temperature. We used this free-energy calculation to evaluate the free energy of the fluid phase to calculate coexistence of the fluid and the crystal phases.

Cluster free energies—Calculating the cluster distribution and coexistence with the bilayer sheets

At low temperature the fluid consists of a distribution of clusters of strongly bound Janus particles. It is virtually impossible to equilibrate these clusters and special strategies are required to obtain thermodynamic information.⁶³ Here, we employed a technique that was already successfully applied to different patchy particles.⁶⁴ For this, we consider a system of N Janus particles in a volume V at temperature T . In the cluster gas phase, these particles form finite clusters with a cluster size distribution N_n , satisfying

$$N = \sum_{n=1}^{\infty} n N_n, \quad (20)$$

where N_n is the number of clusters consisting of n particles. We approximate the free energy of the cluster gas as that of an ideal gas of clusters, plus a hard-sphere contribution:

$$\beta F(N, V, T)$$

$$= \sum_{n=1}^{\infty} N_n \left[\ln N_n - 1 - \ln Z_n + \frac{4\eta - 3\eta^2}{(1 - \eta)^2} \right], \quad (21)$$

where $\eta = \pi \rho \sigma^3 / 6$ is the packing fraction, and Z_n is the partition function of a cluster of size n . In essence, this means that we model the cluster fluid as a fluid of hard spheres with an effective volume given by η/ρ_c , where ρ_c is the total density

of clusters in the system. The partition function of a cluster of size n reads

$$\mathcal{Z}_n = \frac{1}{(4\pi)^n \Lambda^{3n} n!} \int_V d\mathbf{r}^n \int d\Omega^n e^{-\beta U(\mathbf{r}^n, \Omega^n)} c(\mathbf{r}^n, \Omega^n). \quad (22)$$

Here, \mathbf{r}^n and Ω^n denote the positions and orientations of the Janus particles, respectively. The function $c(\mathbf{r}^n, \Omega^n)$ is a constraint function that equals 1 if the n particles form a single continuous cluster, and is 0 otherwise. Since the partition function for a monomer is $\mathcal{Z}_1 = V/\Lambda^3$, this free energy reduces to the Carnahan-Starling hard-sphere free energy in the case where only monomers exist.⁶² Taking the differential of Eq. (21) with respect to the volume yields the pressure P in terms of the cluster distribution:

$$\beta P \sigma^3 = \frac{1 + \eta + \eta^2 - \eta^3}{(1 - \eta)^3} \sum_n \rho_n \sigma^3. \quad (23)$$

The chemical potential is given by

$$\beta \mu = \frac{\beta F}{N} + \frac{\beta P}{\rho}. \quad (24)$$

The equilibrium cluster size distribution can be obtained by minimizing the free energy with respect to N_n , while satisfying the constraint in Eq. (20). This yields

$$\frac{N_n}{N_1^n} = \frac{\mathcal{Z}_n}{\mathcal{Z}_1^n} e^{(n-1)\frac{4\eta-3\eta^2}{(1-\eta)^2}}. \quad (25)$$

The relations between the various \mathcal{Z}_n can be obtained directly from a grand-canonical Monte Carlo (GCMC) simulation.^{64,65} By imposing the constraint of having only a single cluster in a GCMC simulation, the probability $\mathcal{P}(n)$ of observing a cluster of size n reads

$$\frac{\mathcal{P}(n)}{\mathcal{P}(1)} = \frac{\mathcal{Z}_n}{\mathcal{Z}_1} e^{\beta \mu(n-1)}. \quad (26)$$

Hence, the ratio $\mathcal{Z}_n/\mathcal{Z}_1$ can be directly obtained for all n from the GCMC simulation. Note that $\mathcal{Z}_n/\mathcal{Z}_1$ is independent of μ , and we can therefore safely set $\mu = 0$ in our grand-canonical simulations. A few examples of calculated cluster size distributions for Janus particles in our system are shown in Fig. 3.

The requirement that all the particles in the simulation form a single cluster is maintained by simply rejecting any MC moves that would break up the cluster. Since the simulation box needs to be large enough to contain all possible cluster configurations, the probability of inserting a new particle into the cluster is very low unless some form of biased insertion is used. Here, we performed insertions by randomly selecting an existing particle in the cluster, and choosing the position \mathbf{r} of the newly inserted particle uniformly in a shell at distance $\sigma < |\mathbf{r}| < \sigma + \delta$ around the chosen particle. This ensures that there is always at least one nearby particle available for bonding, but areas where multiple shells around existing particles overlap will be sampled multiple times. To correct for this, any insertion performed at a location where k shells overlap is immediately rejected with probability $(k-1)/k$. The modified acceptance rules for inserting and deleting par-

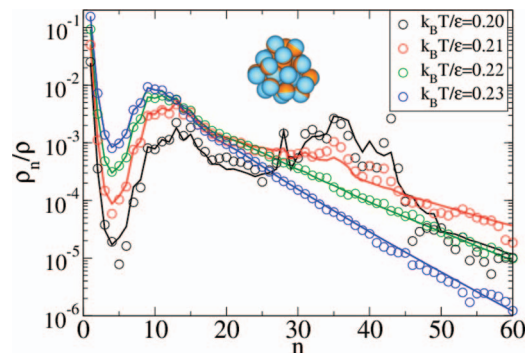


FIG. 3. Cluster size distributions ρ_n/ρ at a density $\rho\sigma^3 = 0.01$ as a function of cluster size n for four different temperatures $k_B T/\epsilon = 0.20$, $k_B T/\epsilon = 0.21$, $k_B T/\epsilon = 0.22$, and $k_B T/\epsilon = 0.23$. Here, ρ_n is the number density of clusters of size n . The lines indicate the results from the single-cluster simulations, and the points are directly obtained from NVT -simulations. Note that the equilibration of large clusters at low temperatures is difficult, likely explaining the deviations for $k_B T/\epsilon = 0.20$. In the inset, a cluster consisting of 28 Janus particles is shown.

ticles read

$$\text{acc}(n \rightarrow n+1) = \min \left[1, \frac{nv}{\Lambda^3(n+1)} e^{\beta[\mu - U(\mathbf{r}^{n+1}, \Omega^{n+1}) + U(\mathbf{r}^n, \Omega^n)]} \right], \quad (27)$$

$$\text{acc}(n+1 \rightarrow n) = \min \left[1, \frac{\Lambda^3(n+1)}{nv} e^{-\beta[\mu + U(\mathbf{r}^n, \Omega^n) - U(\mathbf{r}^{n+1}, \Omega^{n+1})]} \right], \quad (28)$$

where v is the volume of a spherical shell of thickness δ around a particle. Note that insertions and deletions which break the cluster are never allowed.

To properly sample all cluster sizes, we use umbrella sampling:⁵⁷ we run separate simulations for each cluster size n , where only clusters of size n and $n+1$ are allowed. From each simulation we obtain a single ratio $\mathcal{Z}_{n+1}/\mathcal{Z}_n$. Additionally, we use parallel tempering to improve the sampling of different cluster configurations at low temperatures:⁵⁷ within an umbrella sampling window, we simulate clusters for a range of different temperatures and allow switch moves that swap configurations between two systems with different temperatures.

After performing the simulation for each window, we combine the results to calculate \mathcal{Z}_n for every simulated cluster size n , and numerically solve Eq. (25) to obtain the cluster size distribution. We can then use this to calculate the full Helmholtz (and Gibbs) free energy of the system following Eq. (21). Note that the density of the system does not affect the simulations: knowing the individual cluster partition functions allows us to calculate the free energy for any system density where the clusters can be considered as non-interacting.

Successive umbrella sampling

Successive umbrella sampling (SUS)⁶⁶ grand-canonical simulations have been performed for a rather large box size ($L = 14\sigma$) to locate the gas-liquid coexistence curve. SUS

provides the full density probability, $\mathcal{P}(\rho)$ (or equivalently $\mathcal{P}(N)$) of observing the system at density ρ (or equivalently with N particles in the box) at fixed temperature T , chemical potential μ , and volume V . In the SUS method, the explored particle range ($0, N$) is partitioned in many small windows of size ΔN ($\Delta N = 2$ in the present case). For each window, a grand-canonical MC simulation records the number of time a state of N particles is visited. Simulations are complemented with appropriate boundary conditions, constraining the number of particles to remain within the window's range.⁶⁷ Combining the histograms for different windows allows us to evaluate the full density probability, $\mathcal{P}(\rho)$. The coexistence points at fixed T are then obtained by re-weighting $\mathcal{P}(\rho)$ until the two peaks (associated to the coexisting low- and high-density phases) have the same area. Under these conditions, the peak average density provides a precise estimate of the coexistence density.

The evaluation of $\mathcal{P}(N)$ allows us to calculate the coexisting pressure. Indeed $\mathcal{P}(0) = 1/\mathcal{Z}_{gc}$, where $\mathcal{Z}_{gc} = e^{\beta PV}$ is the partition function in the grand-canonical ensemble. From this simple relation one obtains $P = -k_B T \ln \mathcal{P}(0)/V$.

RESULTS

Stable crystals and their structure

The floppy box procedure produces a large number of candidate crystal structures. Most of them do not survive when copied in a large simulation box and equilibrated at the same T and P at which they have been generated in the original floppy box and/or at different T and P values. This significantly reduces the number of candidate crystal structures whose stability needs to be evaluated. In addition, many of the crystals generated in the original floppy box result in the same macroscopic lattice. The application of the criteria listed in Appendix A takes care of the elimination of the duplicate structures.

In the lowest energy structures that we found, Janus particles are packed on a face-centered-cubic (fcc) lattice. In their fully bonded state (i.e., at sufficiently low temperature), there are nine bonds connected to each patch, corresponding to an energy per particle $U/N\epsilon = -4.5$. Groups of four particles form tetrahedra in which the hard-sphere sides are pointed inwards, and the attractive hemispheres are directed outwards (Fig. 4, the orange hemispheres are attractive). Several polymorphs can exist, i.e., there are multiple ways in which the orientations of the particles are pinned on the fcc-lattice. We name all these crystals of type **I**, differentiating with lower case letters the different bonding patterns. In Figs. 4(a)–4(d), the four polymorphs **Ia**–**Id** that were discovered with the floppy box method are depicted. Note that different polymorphs can either have four or eight orientation spots on the unit-sphere, depending on the different ways in which the tetrahedra are oriented.

In addition, we also calculated the distribution of relative patch-orientations $\mathcal{O}(\hat{\mathbf{n}}_i \cdot \hat{\mathbf{n}}_j)$, where $\theta_{ij} \equiv \hat{\mathbf{n}}_i \cdot \hat{\mathbf{n}}_j$ is the inner product between the orientations of all pairs of Janus particles i and j (Fig. 4(e)), so also the relative angles between particles on large distances are incorporated in this distribu-

tion. For crystal **I**, the peak at $\hat{\mathbf{n}}_i \cdot \hat{\mathbf{n}}_j = -0.335$ corresponds to a relative angle of 109.5° , which is a clear fingerprint of the tetrahedral arrangement of the orientations within the crystal structure. The peak near $\hat{\mathbf{n}}_i \cdot \hat{\mathbf{n}}_j = 1.0$ indicates that the orientational order is long-ranged, i.e., particles on different locations point almost exactly in the same direction. To assert the change of the orientations in time, we calculated the time-correlation of particle orientations $\langle \hat{\mathbf{n}}_i(t) \cdot \hat{\mathbf{n}}_i(0) \rangle$ at low temperature (Fig. 4(f)). There are slight differences in the (average) orientational freedom of the particles inside the different polymorphs.

We also found one fully bonded crystal on a hexagonal-close-packed (hcp) lattice, that we name crystal **II**. The unit cell of crystal **II** was found in a small floppy box using eight particles. The unit-cell representation in a rectangular box is shown in Fig. 5(a). Fully bonded, the structure has an energy per particle $U/N\epsilon = -4.125$.

We did not systematically investigate the polymorphs of crystal **II**. In the orientational distribution of crystal **II** (Fig. 5(c)) peaks near $\hat{\mathbf{n}}_i \cdot \hat{\mathbf{n}}_j = -1.0$ and $\hat{\mathbf{n}}_i \cdot \hat{\mathbf{n}}_j = 1.0$ show that particles are pointing in exactly the same, as well as in the opposite directions. The broadness of the distribution confirms that particles in crystal **II** (Fig. 5(c)) have more freedom to rotate than those in crystal **I** (Fig. 4(e)).

In order to calculate the equations of state for the different crystals and to evaluate their melting temperatures, we have performed several standard constant-pressure simulations, sometimes observing spontaneous transitions between different structures. In the course of heating crystal **II** we discovered a transition, characterized by a sudden jump in the internal energy (Fig. 5(b)), around $k_B T/\epsilon = 0.25$ toward a new phase that we name **W**. This new phase, still hcp, has a distinct orientation distribution, showing peaks indicating an increased probability of very specific relative orientations (Fig. 5(c)). A unit cell of the structure is given in Fig. 6(a). Interestingly, structure **W** had not been predicted by the floppy box method. On cooling back, the **W** structure remained metastable down to very low temperature.

Although particles retain their hcp-stacking, like in crystal **II**, the orientations are aligned throughout the crystal in wrinkle-like patterns (Figs. 6(b) and 6(c)). The wrinkles are defined inside the {111} plane of the hcp-crystal and exhibit a typical half-period corresponding to ten particles. In Fig. 6(d) the time-correlation function $\langle \hat{\mathbf{n}}_i(t) \cdot \hat{\mathbf{n}}_i(0) \rangle$ of crystal **W** is shown. Clearly, the correlation fades as the temperature and the structure appears to continuously transform into hcp-packed with random particle orientations (hcp-r). The T -dependence of the relative orientation distributions in crystal **W** is reported in Fig. 6(e). On increasing T , the distribution of the orientations becomes flat, confirming the random orientations of the particles at high T .

To quantify the underlying structure of the crystals (i.e., neglecting orientations) we used the projection of the order parameters \bar{q}_4 and \bar{q}_6 , as described in Ref. 68. This projection is drawn in Fig. 6(f) for both the stable and metastable candidate crystals mentioned above.

In addition to the crystals previously discussed, we identified several other crystals using the floppy box method. We found that for all of these structures the chemical potential

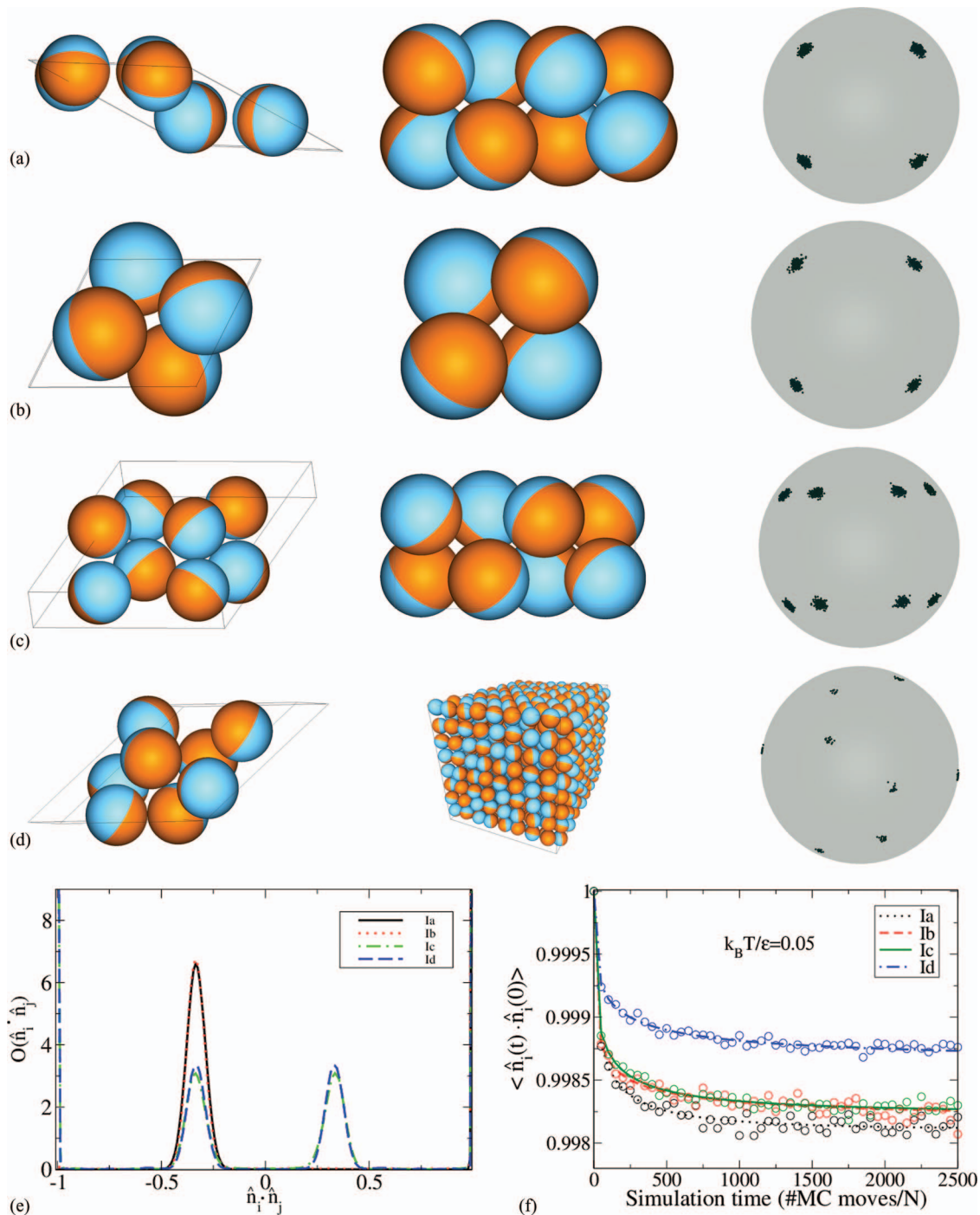


FIG. 4. Different polymorphs of structure **I**, the attractive hemispheres are shown in orange. From top to bottom (a)–(d) **Ia**, **Ib**, **Ic**, and **Id**. From left to right: (i) the unit cell as found in the floppy box; (ii) a representation of the unit cell in a rectangular box; (iii) a distribution of orientations of the particles plotted on the surface of a unit-sphere. (e) Orientations for the polymorphs of **I**, and (f) time-correlation of the particle orientations $\langle \hat{n}_i(t) \cdot \hat{n}_i(0) \rangle$ at low temperature $k_B T/\epsilon = 0.05$ and pressure $\beta P \sigma^3 = 20$, lines are guides to the eye.

(μ) was higher than for **I**, **II**, or **W**, and that they are thus metastable.

For example, crystal **I** (fcc) melts spontaneously into a metastable bilayer-like crystal that also exists on the fcc-lattice when the temperature or the pressure is increased, although **II** (hcp) would be the stable crystal under these conditions. The explanation can be found in the fact that there is a free-energy barrier associated with the change of lattice from **I** to **II**, which makes the pathway from **I** to a metastable crys-

tal more likely. Finally we note that, similar to other known methods to find crystal structures, there is no way to tell with absolute certainty whether all stable crystal structures have been found, since there can exist phases that are not readily captured with small unit cells, like the **W** phase that we found here.

Finally, while performing constant μVT -simulations to investigate the gas-liquid coexistence and critical point, we observed the spontaneous formation of extended aggregates

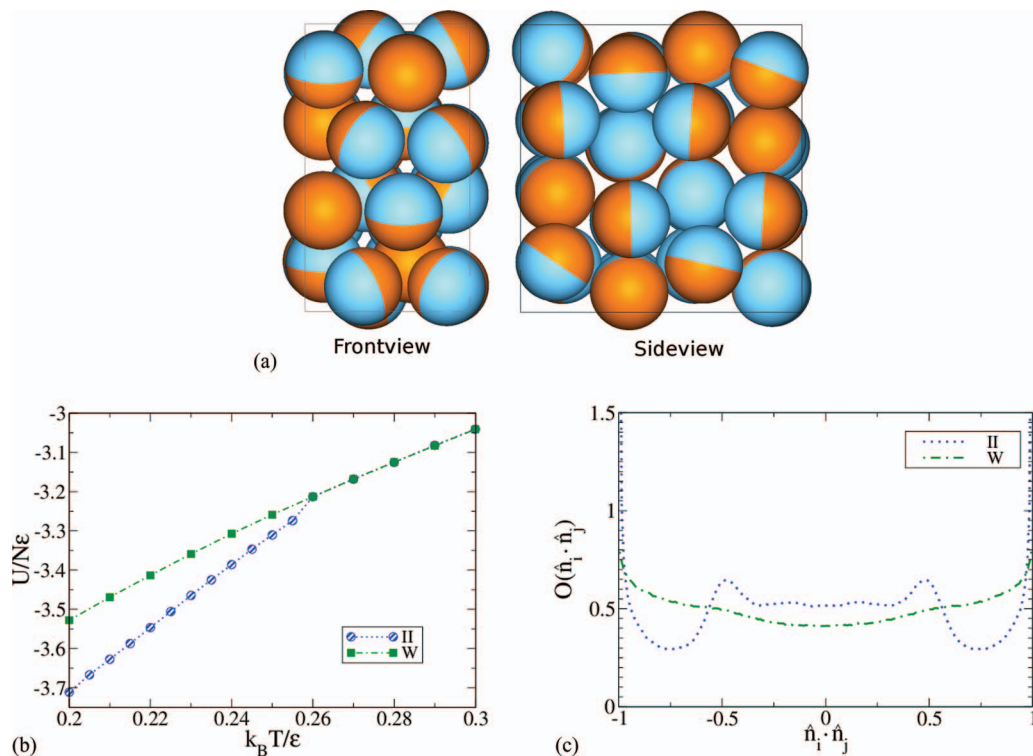


FIG. 5. Unit cell of crystal **II** inside a rectangular box. The attractive hemispheres are shown in orange. From left to right: front view and side-view. (b) Bonding energy per Janus particle versus temperature for structures **II** and **W**. There is a transition from **II** to **W**. Upon cooling, structure **W** did not melt back into **II** but remained meta-stable. (c) Orientation distributions of crystal **II** ($k_B T/\epsilon = 0.19$, $\rho \sigma^3 = 1.172$) and **W** ($k_B T/\epsilon = 0.30$, $\rho \sigma^3 = 1.062$) inside their stability regions.

at $k_B T/\epsilon \leq 0.18$, suggesting the presence of a novel additional ordered phase. From such an aggregate, we were able to extract a unit cell (Fig. 7(a)), which, once duplicated in two directions, comprises a wrinkled bilayer-sheet structure (Fig. 7(b)). A side view of a simulation box containing six wrinkled bilayer sheets connected via shifted periodic boundary conditions is shown in Fig. 7(c).

Crystal relative stability

To evaluate the relative stability of the different crystals and the bilayer sheets, we calculate the P dependence of μ for several T . Results are reported in Figs. 8(a)–8(e). At $k_B T/\epsilon = 0.23$, there is a coexistence between crystal **II** and crystal **W**, as well as a coexistence between the fluid and the bilayer sheets. At $k_B T/\epsilon = 0.21$, the stable phases are the fluid and bilayer sheets at lower pressure and structure **II** at higher pressure. On cooling, at $k_B T/\epsilon = 0.19$, the equation of state of the fluid becomes hard to evaluate directly due to the extreme slow dynamics, and we calculated the free energy using grand-canonical Monte Carlo simulations to calculate the cluster free energy, as described earlier. Among the crystals, **II** is still the most stable structure. On further cooling, at $k_B T/\epsilon = 0.17$, the coexistence point between crystals **I** and **II** appears. Structure **I** becomes more stable at smaller P . At $k_B T/\epsilon = 0.15$, structure **I** is the most stable crystal at all shown pressures. It is interesting to note that the differences in μ between the different crystals is often a small fraction of the thermal

energy $k_B T$, making it particularly difficult to identify the correct stable structure.

Although we did not perform a systematic search to find all the possible polymorphs of crystal **I**, we calculated the free energy for **Ia**–**Id** (Table I). For this, we chose two temperatures T and a density ρ for which the crystal phase was found to be stable. At sufficiently high temperatures, the number of bonds per particle is slightly different for each polymorph. We observed that there are differences in the free energy between the polymorphs of crystal **I**. The most stable candidate that we found was **Ia**, closely followed by **Ib** and **Ic**, and finally crystal **Id** (Fig. 4). By comparing **Id** with **Ia**, we note that reducing the number of orientations inside the unit cell

TABLE I. Calculated potential energies and free energies for different polymorphs of crystal **I**. The calculations in the table were performed at $k_B T/\epsilon = 0.05$ and $k_B T/\epsilon = 0.15$ at constant density $\rho \sigma^3 = 1.070$, well inside the stability region of crystal **I**. Energies refer to the configurations on which the free-energy calculation was performed.

$k_B T/\epsilon$	Crystal	$\rho \sigma^3$	$U/N\epsilon$	$F/Nk_B T$
0.05	Ia	1.070	-4.500	-74.67
0.05	Ib	1.070	-4.500	-74.49
0.05	Ic	1.070	-4.500	-74.42
0.05	Id	1.070	-4.500	-73.68
0.15	Ia	1.070	-4.494	-14.67
0.15	Ib	1.070	-4.492	-14.50
0.15	Ic	1.070	-4.489	-14.43
0.15	Id	1.070	-4.485	-13.70

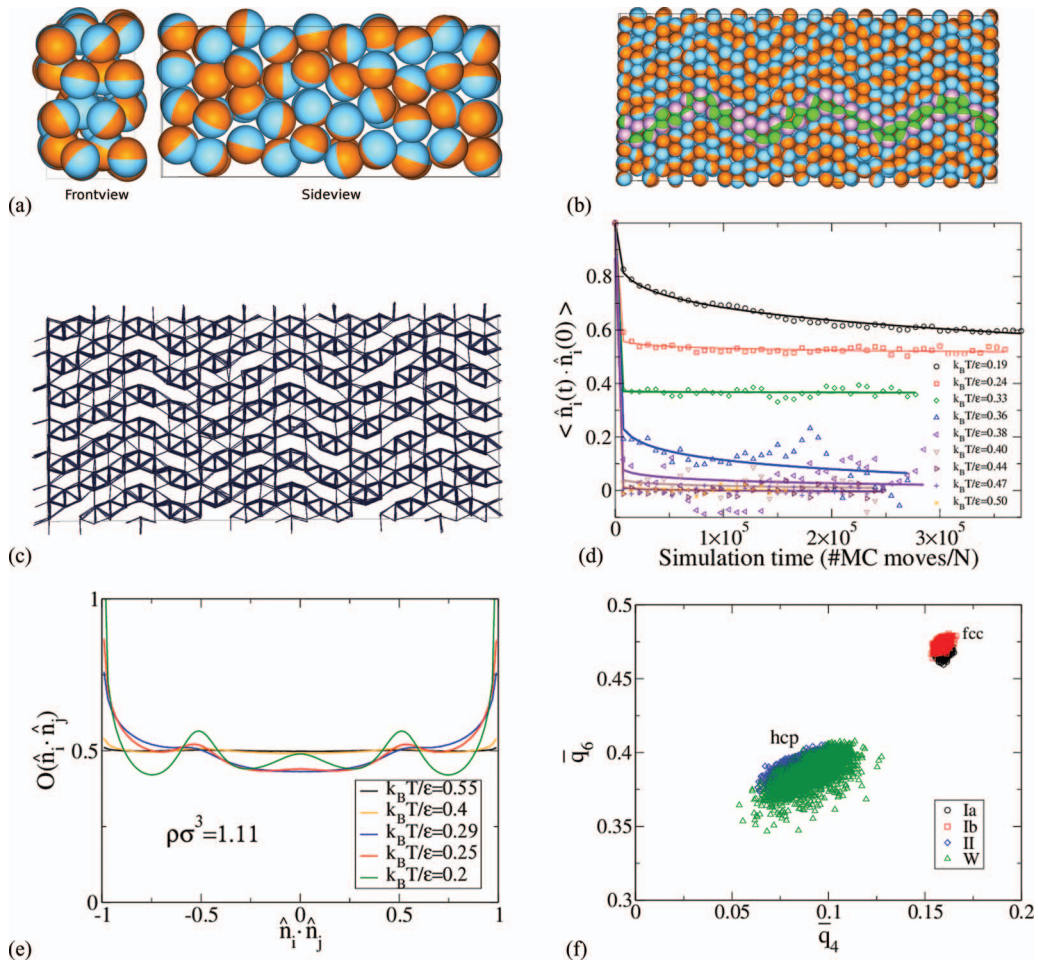


FIG. 6. (a) Unit cell of crystal **W** in a rectangular box. The attractive hemispheres are shown in orange. (b) Crystal **W** inside a rectangular simulation box. One wrinkle is highlighted (attractive hemispheres in green). (c) Bonds inside crystal **W**, depicted with sticks. (d) The correlation of particle orientations ($\langle \hat{\mathbf{n}}_i(t) \cdot \hat{\mathbf{n}}_i(0) \rangle$) between time 0 and time t for different temperatures, all at pressure $P\sigma^3/\epsilon = 4.0$, lines are guides to the eye. (e) The relative orientation distributions $\mathcal{O}(\hat{\mathbf{n}}_i \cdot \hat{\mathbf{n}}_j)$ for **W** at 5 different temperatures at density $\rho\sigma^3 = 1.11$. The distribution becomes flat as the particle orientations become random (hcp-r). (f) The projection of order parameters \bar{q}_4 and \bar{q}_6 , as defined in Ref. 68 for crystals **Ia** ($k_B T/\epsilon = 0.05$, $\rho\sigma^3 = 1.115$), **Ib** ($k_B T/\epsilon = 0.05$, $\rho\sigma^3 = 1.12$), **II** ($k_B T/\epsilon = 0.19$, $\rho\sigma^3 = 1.172$), and **W** ($k_B T/\epsilon = 0.30$, $\rho\sigma^3 = 1.062$).

can lower the free energy with as much as $1 k_B T$ per particle. Interestingly, the more stable polymorphs possess a higher degree of orientational freedom, as can be deduced from the lower correlation between the orientations in Fig. 4(f). This suggests that free energy differences can be ascribed to differences in orientational entropy.

Metastable gas-liquid coexistence

Previous Gibbs-ensemble MC investigations of the same model for interaction range $\Delta = 0.5\sigma$ have shown that Janus particles, modeled with the KF potential, undergo a gas-liquid phase separation.⁵⁵ Unconventionally, the density of the coexisting gas increases on cooling approaching the liquid density

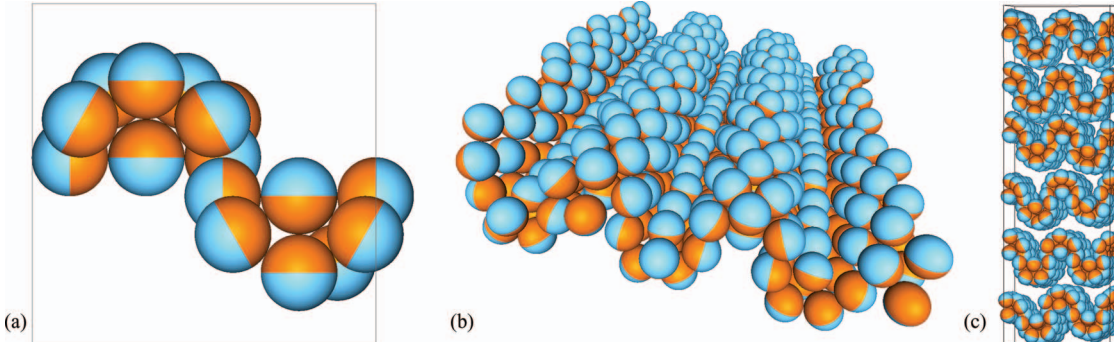


FIG. 7. (a) Unit cell of a wrinkled bilayer sheet consisting of 18 particles. The attractive hemispheres are shown in orange. (b) Top view of a single sheet (in perspective). (c) Snapshot of a simulation box containing 6 wrinkled sheets that are connected via shifted boundary conditions.

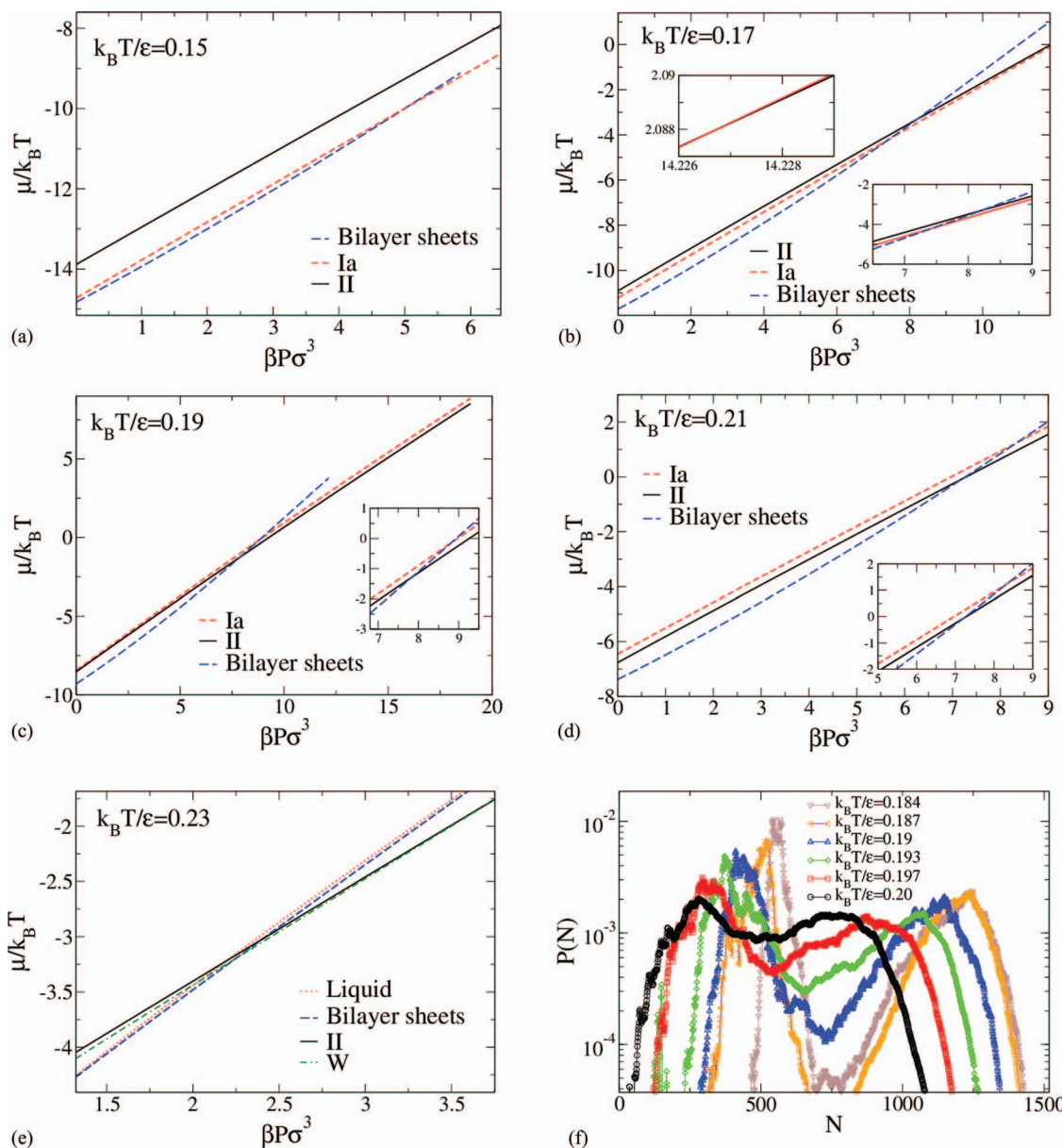


FIG. 8. Chemical potential curves obtained at constant temperatures (a) $k_B T/\epsilon = 0.15$, (b) $k_B T/\epsilon = 0.17$, (c) $k_B T/\epsilon = 0.19$, (d) $k_B T/\epsilon = 0.21$, and (e) $k_B T/\epsilon = 0.23$. Note the coexistence points between **Ia** and **II** at $k_B T/\epsilon = 0.17$, and between **II** and **W** at $k_B T/\epsilon = 0.23$. The coexistence points between the crystals and the bilayer sheets are given as well. The coexistence point between the liquid and the bilayers is only shown here for $k_B T/\epsilon = 0.23$. (f) The probability of finding the system with N particles in the simulation box for different temperatures, as obtained with Successive Umbrella Sampling (SUS)⁶⁶ grand-canonical simulations. As the temperature decreases, the splitting of the peaks gets more pronounced as the (metastable) coexistence region widens.

at low T . Formation of a lamellar phase did not allow for investigation at lower T where a lower critical point could exist.

The anomalous T -dependence of the coexisting gas density was explained in term of a progressive formation in the gas phase of micelles and vesicles, a phase thus characterized by low energy and low entropy per particle (due to the reduction of the orientational degrees of freedom associated to the self-assembly process^{55,69}). A simple and clear mean-field-theoretical model focusing on the competition between self-assembly and phase separation supported such interpretation.⁷⁰ Here we have repeated the calculation of the coexistence curve for the shorter range $\Delta = 0.2\sigma$ by using a more sophisticated methodology which allowed us to evaluate the entire distribution of density fluctuations at

different T and evaluate the coexisting densities. The investigation of an aggregating system is particularly difficult, because the simulation box has to be sufficiently large to allow for the presence of a sufficiently large number of large aggregates. Aggregation also generates a size-independent signal in the density fluctuations, in the window of densities corresponding to a single (or a few) aggregates.⁷¹⁻⁷⁴ For this reason, the box must in addition be sufficiently large so that the contribution of the size-independent signal is negligible. For the present model, we have been forced to work with a cubic box of size $L = 14\sigma$ and investigate the N window $0 \leq N \leq 1500$.

The resulting distribution $\mathcal{P}(N)$, which can be trivially converted to $\mathcal{P}(\rho)$, is shown for different temperatures in

Fig. 8(f). On cooling, both the peak describing the low-density phase and the peak describing the high-density phase move to the right, confirming the unconventional behavior previously found for the $\Delta = 0.5\sigma$ case.⁵⁵ The gas phase is a cluster phase of non-interacting (except for the excluded volume contribution) micelles and vesicles. In this phase, particle orientations are rather well-defined, to satisfy the aggregate geometry. The liquid phase is a homogeneous phase in which particles are orientational disordered. The critical point is located at $k_B T_c/\epsilon = 0.200 \pm 0.002$ (Fig. 8(f)), and $P_c \sigma^3/k_B T_c = 0.004$, while the critical density is $\rho_c \sigma^3 = 0.195 \pm 0.005$. We confirm that the P along the coexistence is negatively sloped in the $P-T$ plane (not shown here), similar as for the $\Delta = 0.5\sigma$ case. This finding, by virtue of the Clausius-Clapeyron equation, indicates that the gas entropy is smaller than the liquid entropy.⁵⁵

Phase diagram

Collecting together all previous results, it is now possible to draw the complete phase diagram of Janus particles. First, the coexistence points were obtained from the calculated chemical potential isotherms Figs. 8(a)–8(e), and the coexistence between the crystal phases, the bilayer sheets, and the fluid were obtained. Subsequently, these points have been selected as starting points of the Kofke integration procedure⁶⁰ to trace the coexistence curves in the $T-P$ (Fig. 9(a)) and $T-\rho$ planes (Fig. 9(b)).

At sufficiently high P yet low T , the maximally bonded crystal I is the most stable (Fig. 9(a)). Above $k_B T/\epsilon \approx 0.15$, structure II becomes more stable despite the fact that it has a lower number of bonds per particle. Entropy becomes a more relevant factor in the free energy and the ability to explore

different orientations compensates for the bond breaking. We recall that, in contrast to I structures, particles in II are on an hcp-lattice. We also recall that on heating, type I structures convert into differently oriented crystals still on an underlying fcc lattice. These heated I structures, which consist of bilayers on the fcc-lattice, are metastable and therefore do not appear on the phase diagram.

Upon further increasing the temperature, structure W becomes more stable than structure II. Although the particles in structure W are still on an hcp-lattice, the orientations form “wrinkles” throughout the crystal. The orientational order progressively decreases on increasing the temperature towards random orientations on an hcp-lattice (hcp-r). We found that the hcp packing remains slightly more stable than the fcc packing for the temperatures mentioned here, although in the limit of high T the fcc crystal should finally become more stable (not shown in the figure), characteristic of a hard-sphere system.⁷⁵

We also find that the wrinkled bilayer sheets are thermodynamically stable for $0.145 \gtrsim k_B T/\epsilon \lesssim 0.23$. Interestingly, the stability field of the wrinkled bilayer sheets is given by a closed shape between the fluid and the crystals. Indeed we find that the wrinkled bilayer sheets phase coexists both with the fluid as well as with the crystal phase. The densities of the fluid followed from the calculation of the cluster distribution. From low to high temperature, the coexisting crystal phase is I, II, or W, respectively. The triple point between the fluid, bilayer sheets, and crystal W is located near $k_B T/\epsilon \approx 0.23$. For temperatures $k_B T/\epsilon \gtrsim 0.23$, the fluid coexists with crystal W, or the hcp-random crystal.

Using the chemical potential of the fluid obtained from the calculations of the cluster distribution, it follows that there is a coexistence between the dilute fluid and the wrinkled bilayer sheets. At low temperatures $k_B T/\epsilon \lesssim 0.2$, the

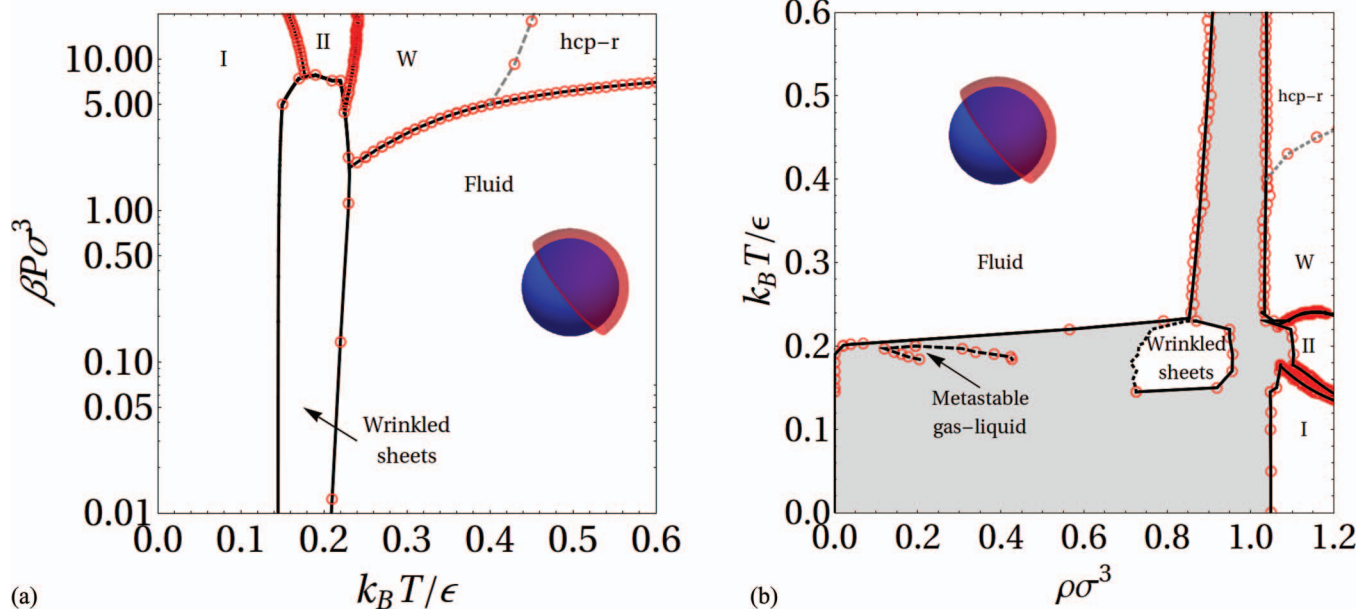


FIG. 9. Phase diagram for Janus particles with range $\Delta = 0.2\sigma$. (a) The temperature-pressure representation. Units are in $k_B T/\epsilon$ and $\beta P \sigma^3$ for temperature and pressure, respectively. The pressure is plotted on a logarithmic scale. The labels denote crystal I, II, W, and the hexagonal-close-packed crystal with random orientations (hcp-r). (b) The representation in the density-temperature plane. Units are in $\rho \sigma^3$ and $k_B T/\epsilon$ for density and temperature, respectively. The dotted line on the left boundary of the wrinkled bilayer sheet phase denotes an upper bound for the fluid-sheet coexistence region.

coexistence pressures are located in the region where it becomes difficult to resolve the equation of state of the bilayer sheets, as described in the Model and Methods section. Moreover, the spaces between the individual sheets can be sufficiently large to contain monomers or even small clusters. In a true equilibrium, these spaces would likely be filled with a gas that has approximately the same density as the coexisting gas. Hence, we expect that inside the fluid-sheet coexistence region, the observed phase would correspond to a mixture of sheets and a dilute gas. In the phase diagram we have indicated with a dotted line an upper bound of this coexistence region. The gas-liquid coexistence calculated from the SUS-simulations is entirely embedded in the region where the fluid and the wrinkled bilayer sheets coexist (Fig. 9(b)) and thus metastable.

CONCLUSIONS

In this article, we focused on the stable crystal phases that can be formed by Janus particles. We implemented the recently proposed floppy box method²¹ complemented by Monte Carlo simulations, free-energy calculations, and thermodynamic integration schemes to investigate these crystals and their stability regions. In addition, we used cluster free-energy calculations and successive umbrella sampling to characterize and calculate the stability of the fluid phases, and to identify a region in which a phase consisting of wrinkled bilayer sheets is stable. Combining all the information, we constructed the equilibrium bulk phase diagram.

The low-temperature crystals are characterized by extensively bonded face-centered-cubic structures, in which there are nine bonds connected to each patch. The low T crystals convert to stable hcp-packed crystals with fewer bonds per patch but more rotational freedom. Interestingly, we found a transition into a phase containing wave-like patterns or “wrinkles” of the particle orientations on the hcp lattice. At high temperatures, hcp- and fcc-crystals with almost random orientations emerge. We emphasize the lesson learned from the **W** structure, which has a very large unit cell (80 particles) and which was not captured by the floppy box method, as only eight particles were used there. All dense stable crystals are based on an underlying fcc or hcp structure. The only lower density structure identified is the wrinkled sheets phase, roughly 25% less dense than the fcc or hcp crystals. It appears that multiple patches are required to generate stable crystal densities even lower than the wrinkled sheets phase.^{8,28–30}

We have confirmed, with a more sophisticated methodology, that Janus particles undergo a gas-liquid phase separation that is metastable with respect to a phase consisting of wrinkled bilayers coexisting with a (dilute) fluid.

The development of the methodology for calculating finite temperature phase diagrams for patchy colloidal particles paves the way for calculations in which the role of the range, the patch size, and the number of patches are carefully investigated. The relative role of these parameters in controlling the crystal phases will then become clear. We plan to do so in the near future. A first exploratory work, showing structures that can form for patch coverage fractions smaller than 0.5, was already published recently.⁹

ACKNOWLEDGMENTS

We gratefully acknowledge support from ERC-226207-PATCHYCOLLOIDS, ITN-234810-COMPOLOIDS, MIUR-PRIN, and from an NWO-VICI grant. We thank Flavio Romano, Gianmarco Munaò, Jeroen Schot, Anjan Gantapara, Joost de Graaf, Nicoletta Gnan, Nikos Koumakis, and Laura Filion for useful discussions.

APPENDIX A: SELECTION AND COMPARISON OF THE CANDIDATE CRYSTAL STRUCTURES

To categorize the equilibrated crystal structures we implemented an algorithm that groups the crystals based on their similarity in density, number of bonds per particle, radial distribution function $g(r_{ij})$, and the relative particle orientation distribution $\mathcal{O}(\hat{\mathbf{n}}_i \cdot \hat{\mathbf{n}}_j)$ of the relative patch-orientations of two particles i and j , which can be at any distance from each other inside the simulation box. To this end, we mutually compared all combinations of structures a and b given a selection criterion C to construct a matrix M_C with elements $m_{ab}^C \in \{0, 1\}$. Specifically, structures a and b are considered identical according to criterion C if $m_{ab}^C = 1$ and not the same if $m_{ab}^C = 0$. To mutually compare the energies, we used the following similarity-criterion:

$$m_{ab}^1 = \begin{cases} 1 & \text{if } |(\langle U_a \rangle - \langle U_b \rangle)/(\langle U_a \rangle + \langle U_b \rangle)| < d_1 \\ 0 & \text{otherwise,} \end{cases} \quad (\text{A1})$$

with d_1 being the maximum relative energy difference allowed for 2 structures to be considered similar. To compare unit cells coming from the small floppy box, where the total number of bonds is low, we can set $d_1 = 0$. After the unit cell is multiplied in 3 directions, we can set it to a low number, e.g., $d_1 \approx 0.05$. For the densities—at a given pressure and temperature—the similarity relation becomes

$$m_{ab}^2 = \begin{cases} 1 & \text{if } |(\langle \rho_a \rangle - \langle \rho_b \rangle)/(\langle \rho_a \rangle + \langle \rho_b \rangle)| < d_2 \\ 0 & \text{otherwise,} \end{cases} \quad (\text{A2})$$

where d_2 is the maximum relative density difference. For unit cells, it generally does not make much sense to compare the densities, since the fluctuations are relatively high due to the low number of particles. For crystals containing more than a few hundred particles, a typical value for $d_2 \approx 0.05$. To compare structural information containing the distances between the centers of mass of the particles for two different structures a and b we compared their radial distribution functions:

$$m_{ab}^3 = \begin{cases} 1 & \text{if } \text{corr}(g_a(r_{ij}), g_b(r_{ij})) > d_3 \\ 0 & \text{otherwise,} \end{cases} \quad (\text{A3})$$

where $\text{corr}(g_a(r_{ij}), g_b(r_{ij}))$ is the normalized cross-correlation function between the two radial distribution functions of structures a and b , and d_3 is the threshold for two structures to be considered similar. To study the orientations of the particles, we used the orientation distribution by plotting the probability $\mathcal{O}_{12}(\hat{\mathbf{n}}_i \cdot \hat{\mathbf{n}}_j)$ to find two particles i and j aligned at angle $\theta_{ij} = \hat{\mathbf{n}}_i \cdot \hat{\mathbf{n}}_j$. Now, we look for similarity in the orientations

of two structures a and b by

$$m_{ab}^4 = \begin{cases} 1 & \text{if } \text{corr}(\mathcal{O}_{12}^a(\hat{\mathbf{n}}_i^a \cdot \hat{\mathbf{n}}_j^a), \mathcal{O}_{12}^b(\hat{\mathbf{n}}_i^b \cdot \hat{\mathbf{n}}_j^b)) > d_4 \\ 0 & \text{otherwise,} \end{cases} \quad (\text{A4})$$

where $\text{corr}(\mathcal{O}_{12}^a(r), \mathcal{O}_{12}^b(r))$ is the normalized cross-correlation function between the two radial distribution functions of structures a and b , and d_4 is the minimal value of the orientational correlation that two structures are ought to have in order to be similar. Typically, d_3 and d_4 were chosen somewhere between 0.9 and 1.0. Finally, we combine all the information above to construct a matrix S of which the elements s_{ab} as follows:

$$s_{ab} = \begin{cases} 1 & \text{if } m_{ab}^C = 1 \quad \forall C \in L \\ 0 & \text{otherwise,} \end{cases} \quad (\text{A5})$$

where L is the list of criteria, in this case $L = \{1, 2, 3, 4\}$. From the matrix S we can identify the structures using that if $S_{ab} = 1$, then a and b belong to the same group of structures. The strong point of this method is that it uses the combination of multiple properties to group structures. If a certain property is not suitable for whatever reason, it can be omitted as long as the other ones guarantee that the structures can still be categorized properly. The exact choice of properties and values for d_n should be chosen carefully for each system, and the different groups of crystals within it.

APPENDIX B: DERIVATION OF THE ORIENTATIONAL FREE ENERGY OF THE REFERENCE SYSTEM

The orientational partition function for a single particle \mathcal{Z}_{or} reads

$$\mathcal{Z}_{\text{or}} = \frac{1}{4\pi\Lambda_r} \int_0^{2\pi} d\phi \int_0^\pi d\psi \sin \psi e^{-\beta U_{\text{ref}}^{\text{or}}(\phi, \psi)}, \quad (\text{B1})$$

where $\Lambda_r = h^2/(8\pi^2 I k_B T)$, and I is the moment of inertia of a Janus particle. Using this definition, the orientational partition function \mathcal{Z}_{or} now becomes

$$\mathcal{Z}_{\text{or}} = \frac{1}{4\pi\Lambda_r} \int_0^{2\pi} d\phi \int_0^\pi d\psi \sin \psi e^{-\beta \lambda_{\text{or}}(1-\cos(\psi))}. \quad (\text{B2})$$

By substituting $dx = d\psi \sin \psi$ we obtain

$$\mathcal{Z}_{\text{or}} = \frac{1}{4\pi\Lambda_r} \int_0^{2\pi} d\phi \int_{-1}^1 dx e^{-\beta \lambda_{\text{or}}(1+x)}. \quad (\text{B3})$$

Using $\beta f = -\ln(\mathcal{Z})$, the reference orientational free energy is given by

$$\beta f_{\text{ref}}^{\text{or}} = -\ln \frac{1}{\Lambda_r} \frac{1 - e^{-2\beta \lambda_{\text{or}}}}{2\beta \lambda_{\text{or}}}. \quad (\text{B4})$$

APPENDIX C: DETAILS CONCERNING AN APPROPRIATE CHOICE OF THE EINSTEIN CRYSTAL

The Einstein crystal that is used as a reference should be carefully chosen, and there should be a continuous, integrable path from the real crystal to the Einstein crystal. We generally used configurations that contained more than 3000 particles. Since our particles interact via a discrete square-well

potential, it occasionally happens that particles in the crystal are located just on the edge of their interaction region or that they are almost touching. As a result, a very small fluctuation in position or rotation can already change its interaction energy with a few $k_B T$ (the energy associated with breaking or forming a bond). If we were to use this crystal directly as an Einstein crystal, high values of the coupling constant lambda would be required to couple the particles to the lattice of the Einstein crystal. This is undesirable because it would require a relatively large number of simulations.

To avoid the need to perform simulations at extremely high values of λ , we slightly adjust the positions of the particles inside the interacting Einstein crystal *before we start the free-energy calculations* in such a way that they are located more towards the center of their interaction regions and sufficiently far from each other to couple them to the ideal Einstein lattice at values of $\beta\lambda = \mathcal{O}(10^4)$. In practice, a good estimate of “sufficiently far” can be obtained from Eqs. (4) and (6). The distance from the center of their Einstein spring corresponding to a reference interaction energy $U_{\text{Ein}}^{\text{tr}} = (k_B T)$ at $\beta\lambda = 10^4$ is 0.01. Analogously, the radial zone, representing the angle between the real orientation and the ideal Einstein orientation, would correspond to $\psi \approx 0.015$. This implies that if the distance between the particles and between a particle and a broken or formed interaction is comparable to this distance/angular, all the particles will be strongly coupled at $\beta\lambda = 10^5$.

To configure the Einstein crystal with the adjusted positions and orientations we perform a constant NVT Monte Carlo simulation where the particles interact via the same Kern-Frenkel square well potential as they do in any other simulation (1). However, we now impose an additional square-shoulder potential with magnitude Π that steadily progresses with simulation time and pushes the particles outside the regions that are on the edges of the interaction wells and close to the hard-cores of other particles:

$$u^{\text{tot}}(\mathbf{r}_{ij}, \hat{\mathbf{n}}_i, \hat{\mathbf{n}}_j) = u^{\text{SSH}}(r_{ij}) \Omega^{\text{SSH}}(\mathbf{r}_{ij}, \hat{\mathbf{n}}_i, \hat{\mathbf{n}}_j) + u^{\text{SW-KF}}, \quad (\text{C1})$$

where $u^{\text{SSH}}(r_{ij})$ is a square-shoulder repulsion potential and $\Omega^{\text{SSH}}(\mathbf{r}_{ij}, \hat{\mathbf{n}}_i, \hat{\mathbf{n}}_j)$ is a function depending on the orientations of the two interacting particles i and j , and $u^{\text{SW-KF}}$ is the square-well Kern-Frenkel potential given by Eq. (1).

$$u^{\text{SSH}}(r_{ij}) = \begin{cases} \Pi & \text{if } \sigma < r_{ij} < \sigma + \delta \\ \Pi & \text{if } \sigma + \Delta - \delta < r_{ij} < \sigma + \Delta + \delta, \\ 0 & \text{otherwise,} \end{cases} \quad (\text{C2})$$

where σ is the hard-sphere diameter and Δ is the interaction range of the square well attractions, and Π is the height of the square shoulder potential:

$$\Omega^{\text{SSH}}(\mathbf{r}_{ij}, \hat{\mathbf{n}}_i, \hat{\mathbf{n}}_j) = \begin{cases} 1 & \text{if } \begin{cases} |\hat{\mathbf{r}}_{ij} \cdot \hat{\mathbf{n}}_i - \cos(\theta)| < \gamma & \text{or} \\ |\hat{\mathbf{r}}_{ji} \cdot \hat{\mathbf{n}}_j - \cos(\theta)| < \gamma \end{cases} \\ 0 & \text{otherwise.} \end{cases} \quad (\text{C3})$$

The height of the shoulder-potential Π was chosen to increase progressively with each step in the process. Typically,

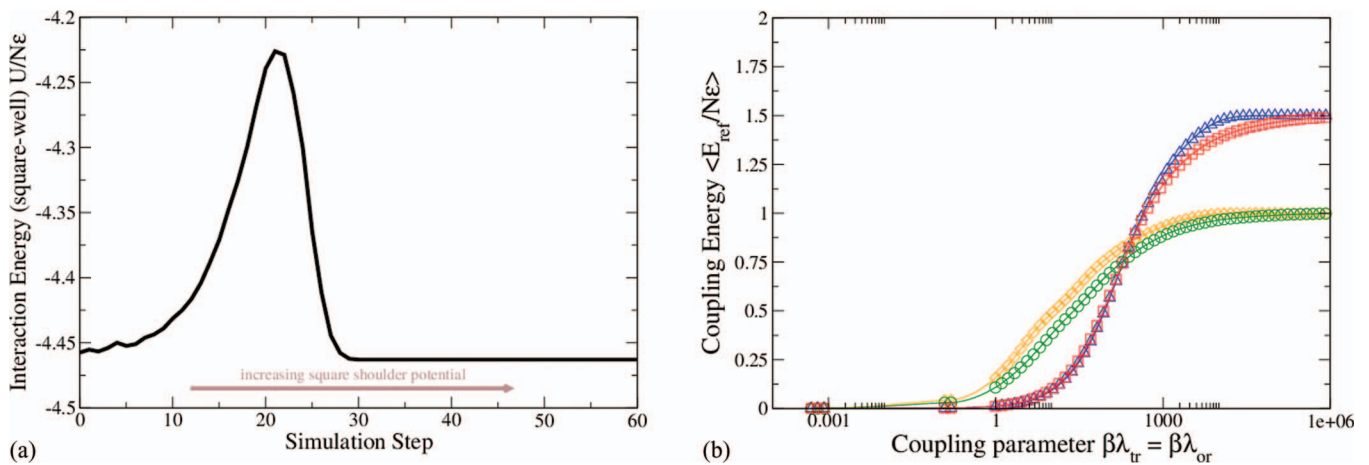


FIG. 10. (a) The interaction energy of the particles inside crystal **Ib** at $k_B T/\epsilon = 0.17$ during the process of adjusting the positions for the Einstein crystal. (b) The translational and rotational coupling energy in the free energy calculation of crystal **II** at $k_B T/\epsilon = 0.21$ as a function of coupling parameter $\beta\lambda$. In this case, $\lambda_{tr} = \lambda_{or}$. Symbols \square (red) and \triangle (blue) denote the translational coupling energy without and with adjusting the particle positions and orientations inside the Einstein crystal, respectively. Symbols \circ (green) and \diamond (yellow) denote the corresponding orientational coupling energies. Note that by adjusting the positions and orientations in the Einstein crystal, the curve approaches the limits of 1.5 for the average translational coupling energy and 1.0 for the average rotational coupling energy corresponding to the perfect Einstein crystal already at lower values of λ .

we used 60 cycles of 300 translation or rotation moves per particle. For each cycle, Π was increased by a factor 1.3, starting from 0.001 at cycle 0 to reach 6864.4 in cycle 60. As a result, particles will be pulled out of regions near the edge of the interaction region. The parameters δ and ω have to be set such that the particles were adjusted in a proper way without totally breaking up the crystal. We used $\delta = 0.015\sigma$ and $\gamma = 0.015$ in this work, but in principle these values have to be set empirically for each system. A typical curve of how the square-well interaction energy changes during the adjustment of the positions for the Einstein crystal is depicted in Fig. 10(a) for the case of crystal **Ib**. In the first cycles, the square shoulder potential Π was very low, and the structure did not change. At somewhat higher values for Π a number of bonds were pushed toward the middle of the interaction region, and some were pushed totally out of it and were broken, resulting in a temporary increase of the interaction energy. At a later stage in the simulation, the broken bonds were formed again. It is desirable that the maximal step size is sufficiently large to overcome the square-shoulder barrier, i.e., greater than 2δ for the translations and greater than 2γ for the rotations.

In Fig. 10(b) we show the integration and the resulting values for ΔF in the case where we used the Einstein crystal without modifying anything, and in the case where the particle positions were adjusted using the potential in Eq. (C1) and the procedure described above.

We stress here that *during* the free-energy calculations the square-shoulder potential is not present. Therefore, for simulations performed at low values of $\lambda \approx 0$, the particle positions and rotations relax to those representing the real crystal of interest. If this were not the case, the obtained free energy would not reflect the crystal of interest, but another one. Hence, it should be carefully checked that the average interaction energy is the same as for an equilibrated configuration of the real crystal of interest.

Finally, we note that at the highest volume fractions, even this strategy will have limited effect, since the particles will be close together and high values of λ are required to avoid an interplay of hard-core exclusions.

- ¹S. C. Glotzer and M. J. Solomon, *Nat. Mater.* **6**, 557 (2007).
- ²A. van Blaaderen, *Nature (London)* **439**, 545 (2006).
- ³A. B. Pawar and I. Kretzschmar, *Macromol. Rapid. Commun.* **31**, 150 (2010).
- ⁴S. Sacanna and D. J. Pine, *Curr. Opin. Colloid Interface Sci.* **16**, 96 (2011).
- ⁵Y. Wang, Y. Wang, D. R. Breed, V. N. Manoharan, L. Feng, A. D. Hollingsworth, M. Weck, and D. J. Pine, *Nature (London)* **491**, 51 (2012).
- ⁶F. Romano and F. Sciortino, *Nat. Mater.* **10**, 171 (2011).
- ⁷F. Romano and F. Sciortino, *Soft Matter* **7**, 5799 (2011).
- ⁸F. Romano and F. Sciortino, *Nat. Commun.* **3**, 975 (2012).
- ⁹G. Munaò, Z. Preisler, T. Vissers, F. Smallenburg, and F. Sciortino, *Soft Matter* **9**, 2652 (2013).
- ¹⁰Q. Chen, S. C. Bae, and S. Granick, *Nature (London)* **469**, 381 (2011).
- ¹¹E. Bianchi, R. Blaak, and C. N. Likos, *Phys. Chem. Chem. Phys.* **13**, 6397 (2011).
- ¹²F. Sciortino and E. Zaccarelli, *Curr. Opin. Solid State Mater. Sci.* **15**, 246 (2011).
- ¹³B. Ruzicka, E. Zaccarelli, L. Zulian, R. Angelini, M. Sztucki, A. Moussaïd, T. Narayanan, and F. Sciortino, *Nat. Mater.* **10**, 56 (2011).
- ¹⁴M. Dijkstra, J. P. Hansen, and P. Madden, *Phys. Rev. Lett.* **75**, 2236 (1995).
- ¹⁵D. de las Heras, J. M. Tavares, and M. M. Telo da Gama, *Soft Matter* **8**, 1785 (2012).
- ¹⁶D. de las Heras, J. M. Tavares, and M. M. Telo da Gama, *Soft Matter* **7**, 5615 (2011).
- ¹⁷D. de las Heras, J. M. Tavares, and M. M. Telo da Gama, *J. Chem. Phys.* **134**, 104904 (2011).
- ¹⁸Z. Zhang, A. S. Keys, T. Chen, and S. C. Glotzer, *Langmuir* **21**(25), 11547 (2005).
- ¹⁹V. Prasad, D. Semwogerere, and E. R. Weeks, *J. Phys.: Condens. Matter* **19**, 113102 (2007).
- ²⁰C. Vega, E. Sanz, J. L. F. Abascal, and E. G. Noya, *J. Phys.: Condens. Matter* **20**, 153101 (2008).
- ²¹L. Filion, M. Marechal, B. van Oorschot, D. Pelt, F. Smallenburg, and M. Dijkstra, *Phys. Rev. Lett.* **103**, 188302 (2009).
- ²²J. de Graaf, R. van Roij, and M. Dijkstra, *Phys. Rev. Lett.* **107**, 155501 (2011).
- ²³J. de Graaf, L. Filion, M. Marechal, R. van Roij, and M. Dijkstra, *J. Chem. Phys.* **137**, 214101 (2012).
- ²⁴P. F. Damasceno, M. Engel, and S. C. Glotzer, *Science* **337**, 453 (2012).

- ²⁵M. Marechal, R. J. Kortschot, A. F. Demirors, A. Imhof, and M. Dijkstra, *Nano Lett.* **10**, 1907 (2010).
- ²⁶R. Ni, A. P. Gantapara, J. de Graaf, R. van Roij, and M. Dijkstra, *Soft Matter* **8**, 8826 (2012).
- ²⁷M. N. van der Linden, J. P. K. Doye, and A. A. Louis, *J. Chem. Phys.* **136**, 054904 (2012).
- ²⁸F. Romano, E. Sanz, and F. Sciortino, *J. Chem. Phys.* **134**, 174502 (2011).
- ²⁹E. G. Noya, C. Vega, J. P. K. Doye, and A. A. Louis, *J. Chem. Phys.* **132**, 234511 (2010).
- ³⁰F. Romano, E. Sanz, P. Tartaglia, and F. Sciortino, *J. Phys.: Condens. Matter* **24**, 064113 (2012).
- ³¹C. Gogelein, F. Romano, F. Sciortino, and A. Giacometti, *J. Chem. Phys.* **136**, 094512 (2012).
- ³²G. Doppelbauer, E. G. Noya, E. Bianchi, and G. Kahl, *Soft Matter* **8**, 7768 (2012).
- ³³L. Filion and M. Dijkstra, *Phys. Rev. E* **79**, 046714 (2009).
- ³⁴E. Bianchi, G. Doppelbauer, L. Filion, M. Dijkstra, and G. Kahl, *J. Chem. Phys.* **136**, 214102 (2012).
- ³⁵A. Walther and A. H. E. Muller, *Soft Matter* **4**, 663 (2008).
- ³⁶K.-H. Roh, D. C. Martin, and J. Lahann, *Nat. Mater.* **4**, 759 (2005).
- ³⁷B. Wang, B. Li, B. Zhao, and C. Y. Li, *J. Am. Chem. Soc.* **130**, 11594 (2008).
- ³⁸C.-H. Chen, R. K. Shah, A. R. Abate, and D. A. Weitz, *Langmuir* **25**, 4320 (2009).
- ³⁹S. Jiang, Q. Chen, M. Tripathy, E. Luijten, K. S. Schweizer, and S. Granick, *Adv. Mater.* **22**, 1060 (2010).
- ⁴⁰A. M. Jackson, J. W. Myerson, and F. Stellacci, *Nat. Mater.* **3**, 330 (2004).
- ⁴¹J. de Graaf, N. Boon, M. Dijkstra, and R. van Roij, *J. Chem. Phys.* **137**, 104910 (2012).
- ⁴²N. Boon, E. C. Gallardo, S. Zheng, E. Eggen, M. Dijkstra, and R. van Roij, *J. Phys.: Condens. Matter* **22**, 104104 (2010).
- ⁴³L. Hong, A. Cacciuto, E. Luijten, and S. Granick, *Langmuir* **24**, 621 (2008).
- ⁴⁴S. Jiang and S. Granick, *Janus Particle Synthesis, Self-assembly and Applications*, edited by S. Jiang and S. Granick (Royal Society of Chemistry, 2012).
- ⁴⁵R. Erhardt, A. Boker, H. Zettl, H. Kaya, W. Pyckhout-Hintzen, G. Krausch, V. Abetz, and A. H. E. Muller, *Macromolecules* **34**, 1069 (2001).
- ⁴⁶M. Torkkeli, R. Serimaa, O. Ikkala, and M. Linder, *Biophys. J.* **83**, 2240 (2002).
- ⁴⁷D. S. Horne, *Curr. Opin. Colloid Interface Sci.* **7**, 456 (2002).
- ⁴⁸L. Hong, A. Cacciuto, E. Luijten, and S. Granick, *Nano Lett.* **6**, 2510 (2006).
- ⁴⁹T. Erdmann, M. Kröger, and S. Hess, *Phys. Rev. E* **67**, 041209 (2003).
- ⁵⁰W. L. Miller and A. Cacciuto, *Phys. Rev. E* **80**, 021404 (2009).
- ⁵¹Q. Chen, J. Yan, J. Zhang, S. C. Bae, and S. Granick, *Langmuir* **28**, 13555 (2012).
- ⁵²J. Yan, M. Bloom, S. C. Bae, E. Luijten, and S. Granick, *Nature (London)* **491**, 578 (2012).
- ⁵³N. Kern and D. Frenkel, *J. Chem. Phys.* **118**, 9882 (2003).
- ⁵⁴A. Giacometti, F. Lado, J. Largo, G. Pastore, and F. Sciortino, *J. Chem. Phys.* **132**, 174110 (2010).
- ⁵⁵F. Sciortino, A. Giacometti, and G. Pastore, *Phys. Rev. Lett.* **103**, 237801 (2009).
- ⁵⁶D. Frenkel and A. J. C. Ladd, *J. Chem. Phys.* **81**, 3188 (1984).
- ⁵⁷D. Frenkel and B. Smit, *Understanding Molecular Simulations: From Algorithms to Applications* (Academic Press, 2002).
- ⁵⁸H. Akima, *ACM Trans. Math. Softw.* **4**, 148 (1978).
- ⁵⁹R. Eppenga and D. Frenkel, *Mol. Phys.* **52**, 1303 (1984).
- ⁶⁰D. A. Kofke, *J. Chem. Phys.* **98**, 4149 (1993).
- ⁶¹U. M. Ascher and L. R. Petzold, *Computer Methods for Ordinary Differential Equations and Differential-Algebraic Equations*, 1st ed. (Society for Industrial and Applied Mathematics, Philadelphia, PA, 1998).
- ⁶²N. F. Carnahan and K. E. Starling, *J. Chem. Phys.* **51**, 635 (1969).
- ⁶³R. Fantoni, A. Giacometti, F. Sciortino, and G. Pastore, *Soft Matter* **7**, 2419 (2011).
- ⁶⁴D. J. Kraft, R. Ni, F. Smallenburg, M. Hermes, K. Yoon, D. A. Weitz, A. van Blaaderen, J. Groenewold, M. Dijkstra, and W. K. Kegel, *Proc. Natl. Acad. Sci. U.S.A.* **109**, 10787 (2012).
- ⁶⁵R. Pool and P. G. Bolhuis, *J. Phys. Chem. B* **109**, 6650 (2005).
- ⁶⁶P. Virnau and M. Müller, *J. Chem. Phys.* **120**, 10925 (2004).
- ⁶⁷R. L. C. Vink, J. Horbach, and K. Binder, *Phys. Rev. E* **71**, 011401 (2005).
- ⁶⁸W. Lechner, C. Dellago, and P. G. Bolhuis, *Phys. Rev. Lett.* **106**, 085701 (2011).
- ⁶⁹F. Sciortino, A. Giacometti, and G. Pastore, *Phys. Chem. Chem. Phys.* **12**, 11869 (2010).
- ⁷⁰J. P. K. Doye, A. A. Louis, I.-C. Lin, L. R. Allen, E. G. Noya, A. W. Wilber, H. C. Kok, and R. Lyus, *Phys. Chem. Chem. Phys.* **9**, 2197 (2007).
- ⁷¹L. Rovigatti, J. Russo, and F. Sciortino, *Phys. Rev. Lett.* **107**, 237801 (2011).
- ⁷²M. A. Floriano, E. Caponetti, and A. Z. Panagiotopoulos, *Langmuir* **15**, 3143 (1999).
- ⁷³F. Lo Verso, A. Z. Panagiotopoulos, and C. N. Likos, *Phys. Rev. E* **79**, 010401 (2009).
- ⁷⁴A. Z. Panagiotopoulos, M. A. Floriano, and S. K. Kumar, *Langmuir* **18**, 2940 (2002).
- ⁷⁵P. G. Bolhuis, D. Frenkel, S.-C. Mau, and D. A. Huse, *Nature (London)* **388**, 235 (1997).